Supporting Information

Acoustic Cavitation Engineering of LLZTO-Coated Separators for Moisture-Resistant Lithium Metal Batteries

Yuka Fadana,[†] Yuan-Ting Hung,[†] Hsin-Wei Chen[‡], Chien-Hsing Lee[‡], and Ru-Shi Liu,[†,]*

[†]Department of Chemistry and the Advanced Research Center for Green Materials Science and Technology, National Taiwan University, Taipei 10617, Taiwan

[‡]Foresight Energy Technologies Co. Ltd., Tainan 744092, Taiwan

Corresponding Author

rsliu@ntu.edu.tw (Ru-Shi Liu)

Experimental Methods

Preparation of garnet-type $Li_{6.75}La_3Zr_{1.75}Ta_{0.25}O_{12}$ (LLZTO) powder.

Garnet-type $Li_{6.75}La_3Zr_{1.75}Ta_{0.25}O_{12}$ (LLZTO) nanoparticles were synthesized through a solid-state reaction following a procedure previously established by our group.[1] Stoichiometric amounts of LiOH (98%, Alfa Aesar), La_2O_3 (99.9%, Sigma-Aldrich), ZrO_2 (99.7%, Alfa Aesar), and Ta_2O_5 (99.0%, Sigma-Aldrich) were used as starting precursors. Before mixing, LiOH and La_2O_3 were preheated at 200°C for 6 hours and at 900°C for 24 hours, respectively, to remove adsorbed moisture and carbonates. All precursors were weighed to achieve the target atomic molar ratio, with an additional 10 wt% excess of LiOH introduced to compensate for lithium volatilization during high-temperature sintering.

The precursor mixture was transferred into a zirconia ball-milling jar and milled for 12 h to achieve a homogeneous powder. The resulting slurry was dried at 70°C for 12 h, ground, and subsequently sintered in an alumina crucible at 900°C for 12 h to obtain phase-pure cubic LLZTO. The sintered bulk was then subjected to a second 12 h ball-milling step to produce fine LLZTO nanoparticles suitable for subsequent coating processes.

Preparation of S-LLZTO.

The as-prepared LLZTO nanoparticles were dispersed in deionized (DI) water to obtain a 10 mg/mL suspension. Acoustic cavitation treatment was then applied using a bath sonicator operating at 20–40 kHz (maximum output power: 161 W). To examine the influence of cavitation duration, the suspension was bath-sonicated for 10, 20, and 30 min, with the operating power kept constant and the treatment conducted at room temperature (25°C). These treatment durations were selected to examine the time-dependent evolution of surface reconstruction, particle deagglomeration, and surface charge modulation under otherwise identical cavitation conditions. In the present study, cavitation time was the primary variable, whereas the ultrasonic power and temperature were maintained constant to isolate the effect of treatment duration on the surface properties of LLZTO. Following cavitation treatment, the LLZTO suspension was centrifuged at

8000 rpm for 10 min to collect the sonication S-LLZTO. The recovered powder was subsequently dried in a high-vacuum chamber at room temperature overnight to remove residual moisture.

Fabrication of S-LLZTO–Coated Polypropylene Separators.

Pristine polypropylene (PP) and Al_2O_3-coated PP (PP–Al_2O_3) separators were supplied from *Foresight Energy Technologies Co. Ltd* and used as received as reference samples. LLZTO-based coated separators were prepared by casting a ceramic slurry onto the PP substrate. In a typical procedure, either as-synthesized LLZTO or sonication-treated LLZTO (S-LLZTO) was dispersed in a mixed solvent consisting of isopropyl alcohol (IPA, 99%, Sigma-Aldrich) and deionized water with a volume ratio of 1:9. A silicon-based wetting agent (SN600, Taiwan Surfactant Corp.) and an acrylic acid–based binder (LA166, Meishan Indigo Technology Co., Ltd., China) were then added as the wetting additive and binder, respectively. The composition of the coating slurry was adjusted to 28.8 wt% LLZTO or S-LLZTO, 0.2 wt% wetting agent, 3 wt% acrylic binder, and 68 wt% IPA/H_2O mixed solvent. The mixture was magnetically stirred at room temperature for 8 h to obtain a homogeneous slurry.

For coating, a PP separator sheet was affixed horizontally to a glass plate with adhesive tape, and the LLZTO (or S-LLZTO) slurry was poured onto the surface and spread uniformly in one direction using a wire-bar coater to form a thin wet layer. The coated separator was then dried in a convection oven at 50°C for 10 min to remove the solvent, yielding the LLZTO-coated PP (PP–LLZTO) or sonication-reconstructed LLZTO-coated PP (PP–S-LLZTO) separator. All electrochemical measurements in this work were conducted using pristine PP, commercial PP–Al_2O_3, and the laboratory-prepared PP–LLZTO and PP–S-LLZTO separators for comparison.

Cathode and Anode Preparation.

The $LiFePO_4$ (LFP) cathode was fabricated by first blending LFP (active material), polyvinylidene fluoride (PVDF, binder), and KS6 conductive carbon in a weight ratio of 75:5:20. The dry components were manually ground in a mortar for 10 min to achieve a uniform mixture. The resulting powder was transferred into a glass vial, and N-methyl-2-pyrrolidone (NMP, 99.8%, Sigma-Aldrich) was added as the solvent to form a slurry. The slurry was homogenized by ball

milling for 15–20 min and then cast onto aluminum foil using a doctor blade. The coated electrodes were dried under vacuum at 120°C overnight. The resulting cathode loading was approximately 2.5 mg cm^{-2}.

Lithium metal foil was used as the anode in both symmetric-cell and full-cell configurations. Before assembly, the Li foil was gently polished to remove surface oxide layers and punched into disks matching the separator size.

Material characterizations.

The structural characteristics of the pristine and sonication-reconstructed LLZTO nanoparticles were examined using X-ray diffraction (XRD, Bruker D2 Phaser) equipped with Cu Kα radiation (λ = 1.5406 Å). Diffraction patterns were collected at 30 kV and 30 mA over a 2θ range of 10–80° with a scan rate of 0.03° s^{-1} to evaluate phase purity, peak broadening, and the retention of the cubic garnet structure. Thermogravimetric analysis (TGA; Rigaku TG-DTA8120) was conducted under nitrogen from room temperature to 500°C at a heating rate of 10°C/min to quantify moisture adsorption, assess thermal stability, and compare mass losses attributable to carbonate-related surface contaminants. The particle size distribution and zeta potential of Al_2O_3, LLZTO, and S-LLZTO dispersions were determined using dynamic light scattering (Malvern Zetasizer Nano) at 25°C with a fixed backscattering angle of 173°, allowing analysis of cavitation-driven deagglomeration, hydrodynamic diameter evolution, and surface-charge modulation. Surface wettability of the PP, PP–Al_2O_3, and PP–S-LLZTO separators was characterized through static contact-angle measurements (KRÜSS DSA) using 3 μL DI-water droplets recorded within the first 2 s to minimize evaporation and spreading artifacts. Additionally, the surface morphology, filler dispersion, and coating integrity of the separators were examined using scanning electron microscopy (SEM, JEOL JSM-6700F). Samples were mounted on conductive stubs, sputter-coated with a thin Pt layer, and imaged at 5–10 kV at various magnifications to evaluate coating coverage, LLZTO particle distribution, and structural differences induced by sonication. Raman spectroscopy was carried out using a ThermoFisher DXR Raman spectrometer equipped with a 532 nm laser. Fourier transform infrared (FTIR) spectroscopy was performed using a Perkin-Elmer 5102-62 spectrometer to further examine the carbonate-related surface species before and after cavitation treatment. X-ray photoelectron spectroscopy (XPS) analysis was conducted on a

ULVAC PHI 5000 Versa Probe III using Al Kα radiation (hν = 1486.6 eV) to investigate the surface chemical states of pristine LLZTO and S-LLZTO. The surface-layer structure and local lattice features were further examined by High-Resolution Transmission Electron Microscopy (HRTEM, JEOL JEM 1200EX II). Collectively, these structural, thermal, morphological, and interfacial characterization techniques provided a comprehensive evaluation of the physicochemical modifications induced by acoustic cavitation and their impact on moisture sensitivity, coating uniformity, and overall separator performance.

Electrochemical performance evaluation.

The electrochemical properties of pristine PP, PP–Al_2O_3, PP–LLZTO, and PP–S-LLZTO separators were systematically evaluated through impedance and galvanostatic cycling measurements. Ionic transport behavior was characterized using electrochemical impedance spectroscopy (EIS) in stainless-steel/separator/stainless-steel symmetric cells on an Autolab PGSTAT30 system, with measurements collected across a frequency range of 0.1 Hz–10^7 Hz using a 10 mV perturbation. The resulting Nyquist plots were fitted with ZView software to determine bulk and interfacial resistances. Oxidative stability was examined via linear sweep voltammetry (LSV) at a scan rate of 0.1 mV s^{-1} in Li/separator/stainless-steel configurations. Lithium-ion transference behavior was assessed using chronoamperometry, in which a 10 mV potential step was applied for 1000 s to monitor the transition from the initial to the steady-state current. Lithium plating–stripping stability was evaluated in Li/separator/Li symmetric cells at room temperature using a Chroma 17216M-10-6 tester, operated at a constant current density (0.1 mA cm^{-2}) until failure; notably, PP–S-LLZTO demonstrated stable cycling for more than 800 h. Full-cell electrochemical performance was investigated using $LiFePO_4$ cathodes paired with lithium metal anodes, cycled at 1 C on an AcuTech BAT-750B system at room temperature, thereby enabling comparison of capacity retention and rate capability across different separator systems. All cell assembly procedures were performed inside an Ar-filled glovebox with H_2O and CO_2 levels maintained below 1 ppm to prevent air- or moisture-induced degradation.

The ionic conductivity (σ) of each separator was calculated according to

$$\sigma = \frac{L}{R \times A}$$

where L is the separator thickness, $R$is the bulk resistance obtained from the high-frequency intercept of the Nyquist plot after fitting with ZView, and A is the effective contact area of the stainless-steel electrode. .

The lithium-ion transference number (t_{Li^+}) was calculated using the Bruce–Vincent–Evans equation

$$t_{Li^+} = \frac{I_s(\Delta V - I_0 R_0)}{I_0(\Delta V - I_s R_s)}$$

where $I_0$and $I_s$are the initial and steady-state currents, respectively, $\Delta V$is the applied DC polarization voltage, and $R_0$and $R_s$are the interfacial resistances measured before and after polarization.

The specific charge/discharge capacity (Q) was calculated using

$$Q = \frac{I \times t}{m}$$

where I is the applied current, t is the charge or discharge time, and m is the mass of active material in the cathode.

The coulombic efficiency (CE) was calculated according to

$$CE(\%) = \frac{Q_c}{Q_d} \times 100$$

where $Q_c$and $Q_d$are the charge and discharge capacities, respectively.

The capacity retention after cycling was calculated using

$$\text{Capacity retention}(\%) = \frac{Q_n}{Q_1} \times 100$$

where $Q_n$is the discharge capacity at the n-th cycle and $Q_1$is the discharge capacity at the first cycle.

Supporting Figures and Tables

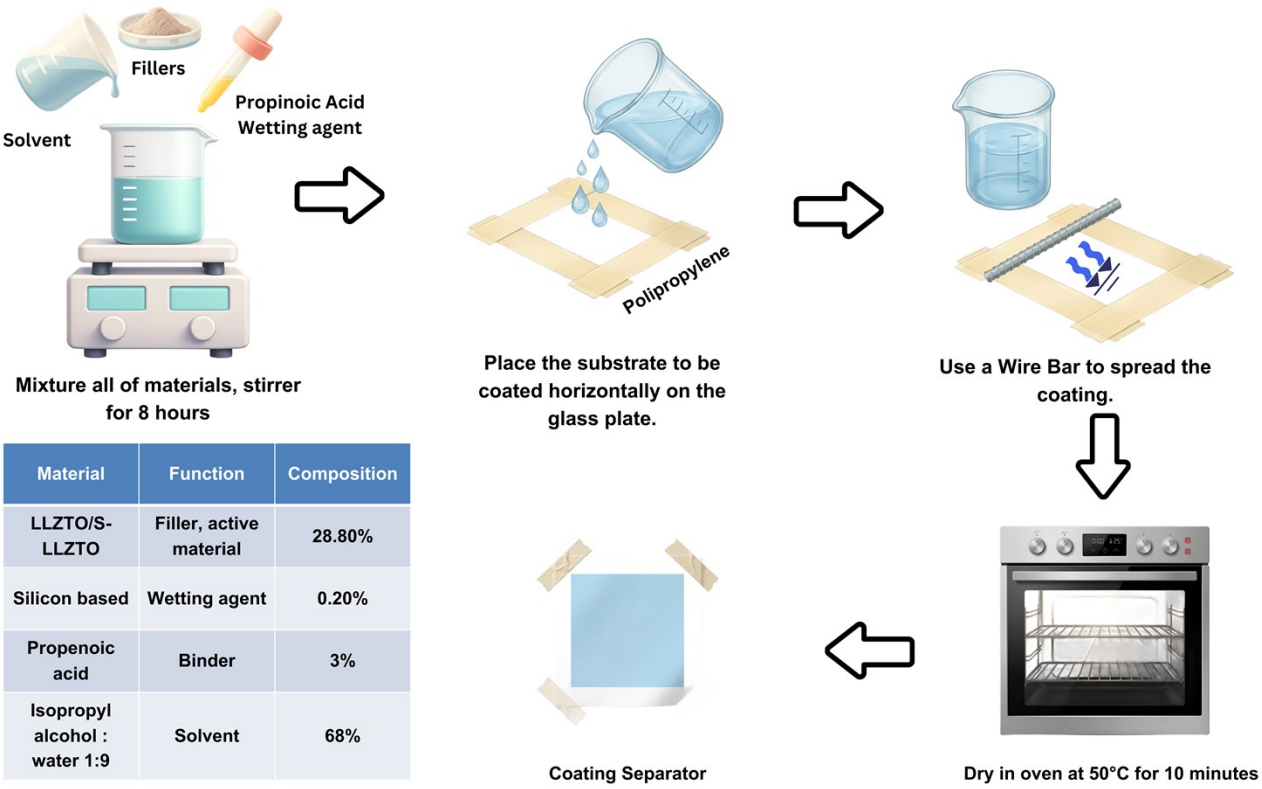

Material	Function	Composition
LLZTO/S-LLZTO	Filler, active material	28.80%
Silicon based	Wetting agent	0.20%
Propenoic acid	Binder	3%
Isopropyl alcohol : water 1:9	Solvent	68%

Figure S1. Schematic of the experimental procedure for preparing the coated polypropylene separator.

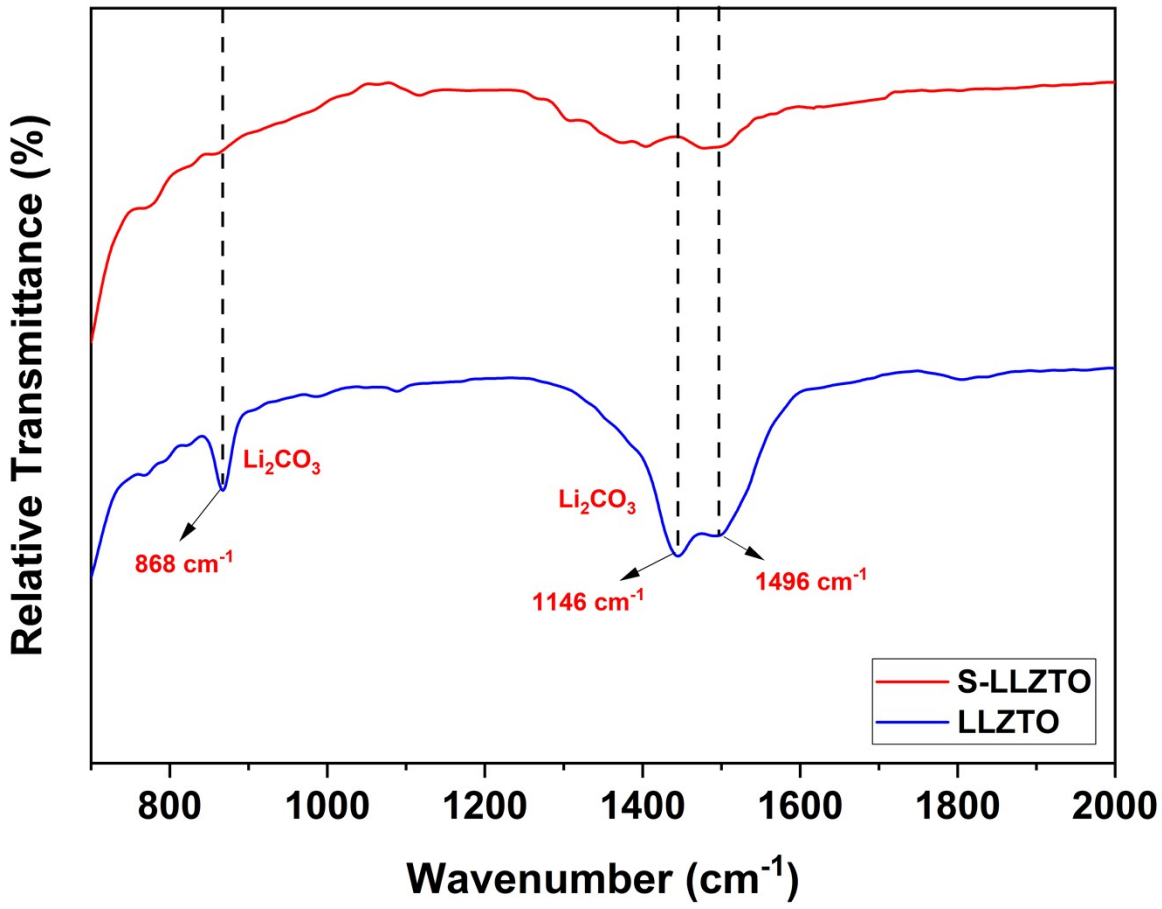

Figure S2. FTIR spectra of pristine LLZTO and cavitation-treated S-LLZTO, showing the attenuation of carbonate-related vibrational bands after acoustic cavitation.

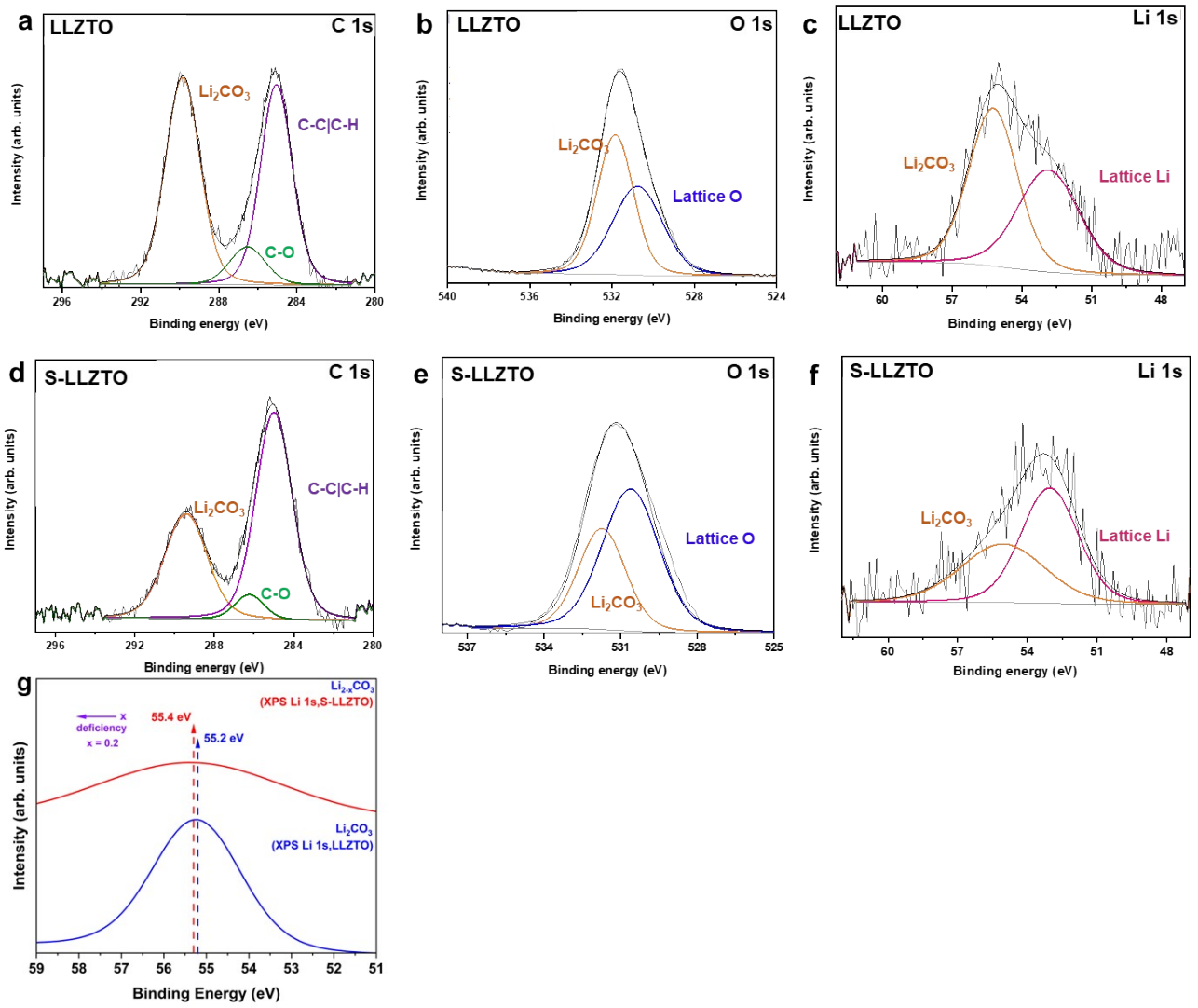

Figure S3. High-resolution XPS spectra of pristine LLZTO and cavitation-treated S-LLZTO: **(a)** C 1*s* spectrum of pristine LLZTO, showing carbonate-related and C–C/C–H contributions; **(b)** O 1*s* spectrum of pristine LLZTO, showing carbonate- and lattice oxygen-related components; **(c)** Li 1*s* spectrum of pristine LLZTO, showing contributions from surface Li_2CO_3 and lattice Li; **(d)** C 1*s* spectrum of S-LLZTO after acoustic cavitation; **(e)** O 1*s* spectrum of S-LLZTO after acoustic cavitation; and **(f)** Li 1*s* spectrum of S-LLZTO after acoustic cavitation. Compared with pristine LLZTO, the spectra of S-LLZTO show a reduced carbonate-related contribution, confirming the cavitation-induced modification of the surface chemical environment. (g) Schematic comparison of the Li 1*s* binding-energy shift between pristine LLZTO and S-LLZTO.

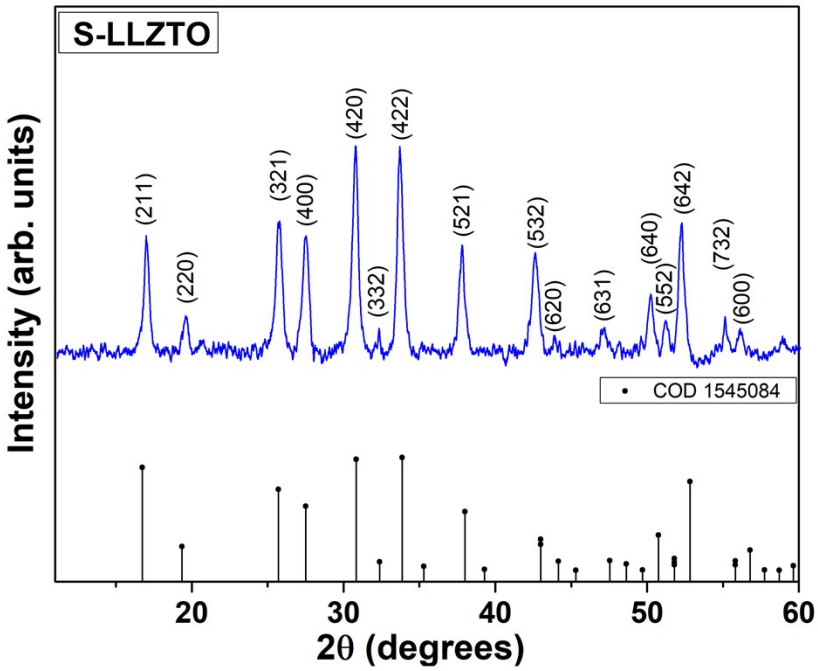

Figure S4. XRD pattern of S-LLZTO compared with the reference garnet phase, confirming the crystalline structure and phase purity after acoustic cavitation treatment.

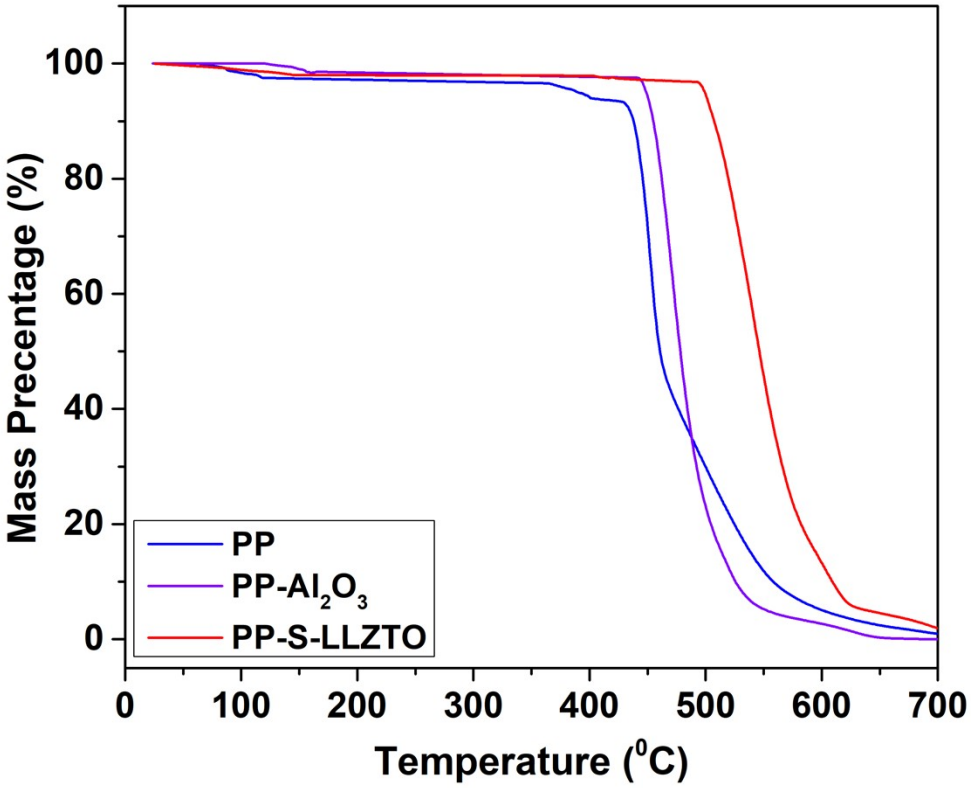

Figure S5. TGA curves of PP, PP–Al_2O_3, and PP–S-LLZTO separators showing differences in thermal decomposition behavior, with the S-LLZTO coating enhancing thermal stability relative to pristine and Al_2O_3-coated PP.

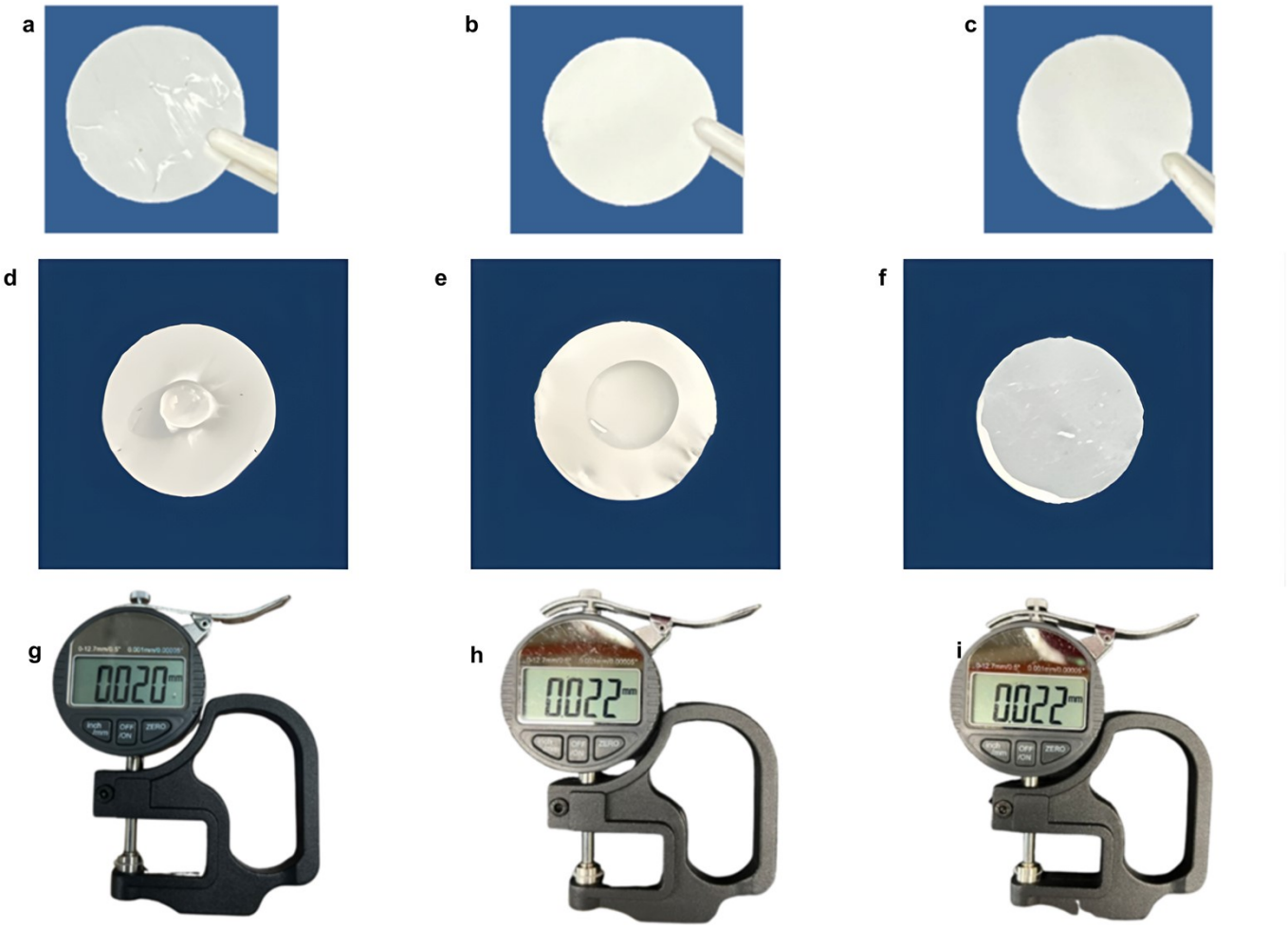

Figure S6. Appearance of **(a)** PP, **(b)** PP–Al_2O_3, and **(c)** PP–S-LLZTO separators. Appearance of **(d)** PP, **(e)** PP–Al_2O_3, and **(f)** PP–S-LLZTO after liquid uptake test using water. Thickness of **(g)** PP, **(h)** PP–Al_2O_3, and **(i)** PP–S-LLZTO.

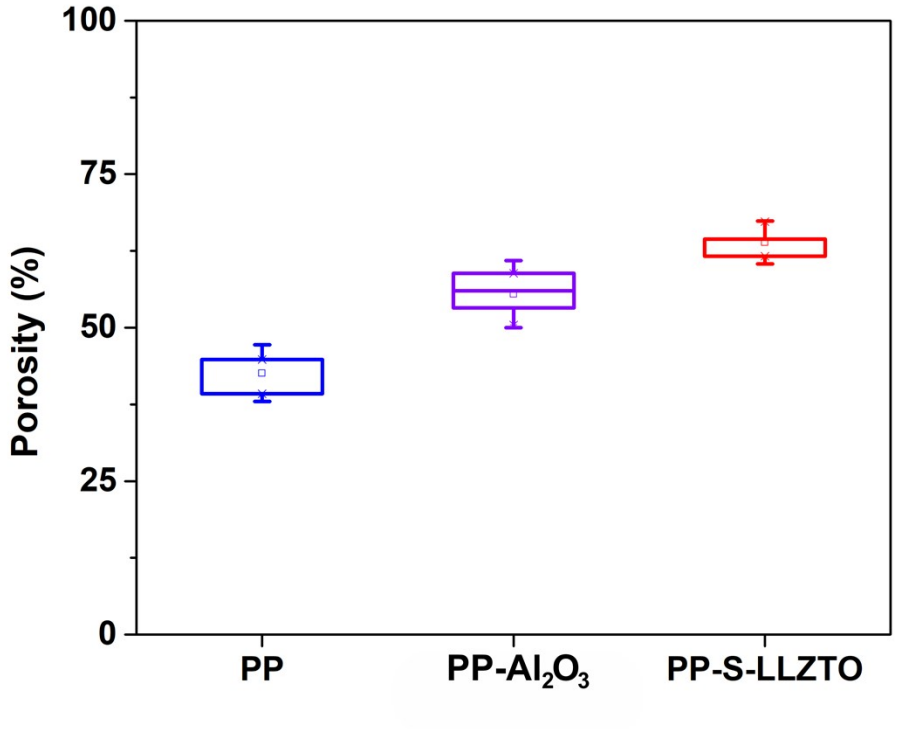

Figure S7. Porosity comparison of PP, PP–Al_2O_3, and PP–S-LLZTO separators, showing increased porosity in the coated samples, with the S-LLZTO layer providing the highest porosity among the three.

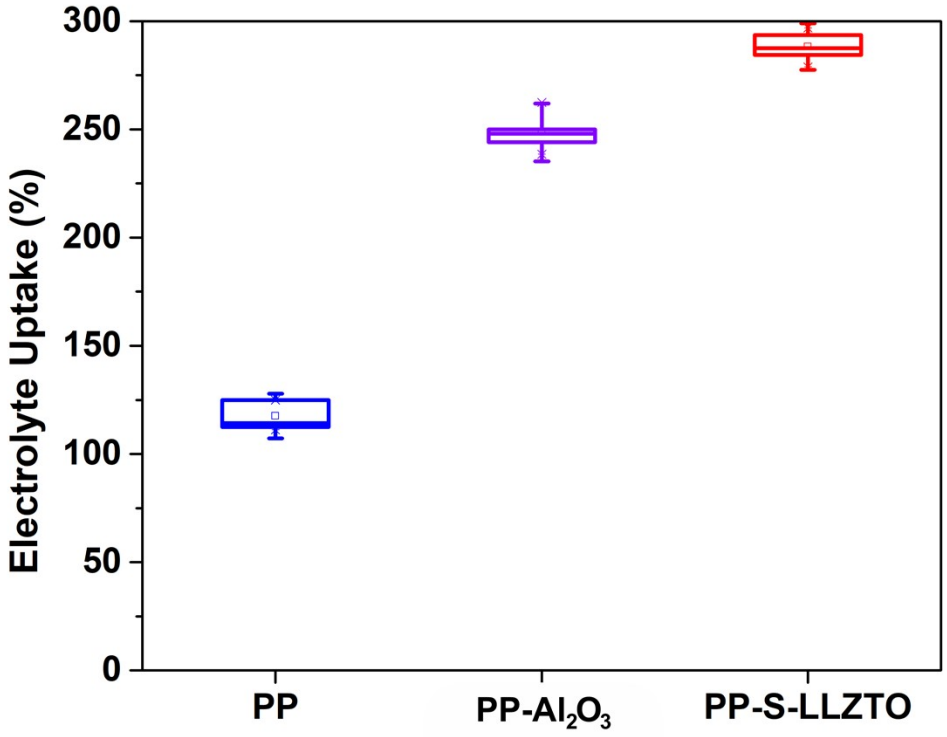

Figure S8. Electrolyte uptake of PP, PP–Al_2O_3, and PP–S-LLZTO separators, showing significantly enhanced absorption in the coated samples, with PP–S-LLZTO exhibiting the highest electrolyte uptake.

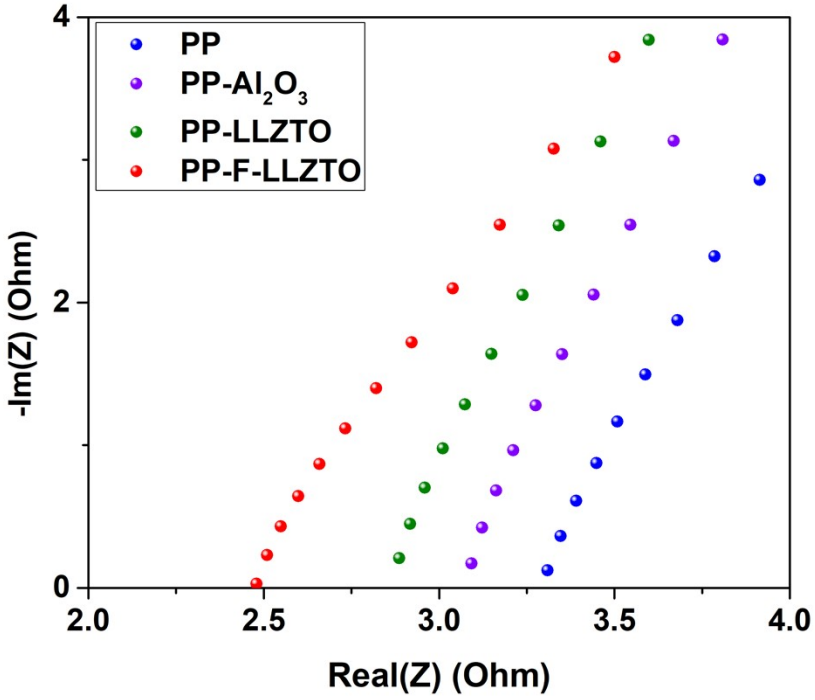

Figure S9. Zoomed-in Nyquist plots of PP, PP–Al_2O_3, PP–LLZTO, and PP–S-LLZTO separators, highlighting the reduced interfacial resistance achieved by LLZTO and S-LLZTO–based coatings compared to pristine PP and PP–Al_2O_3 separators.

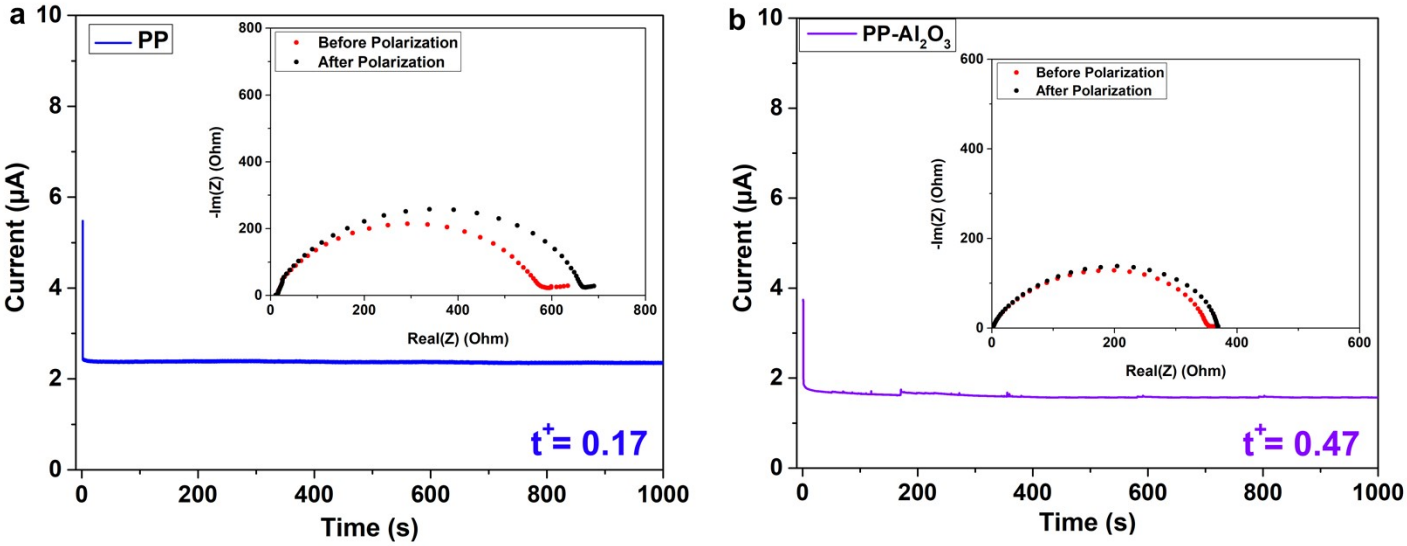

Figure S10. Chronoamperometry profiles and corresponding EIS spectra before and after polarization for **(a)** PP and **(b)** PP–Al_2O_3 separators.

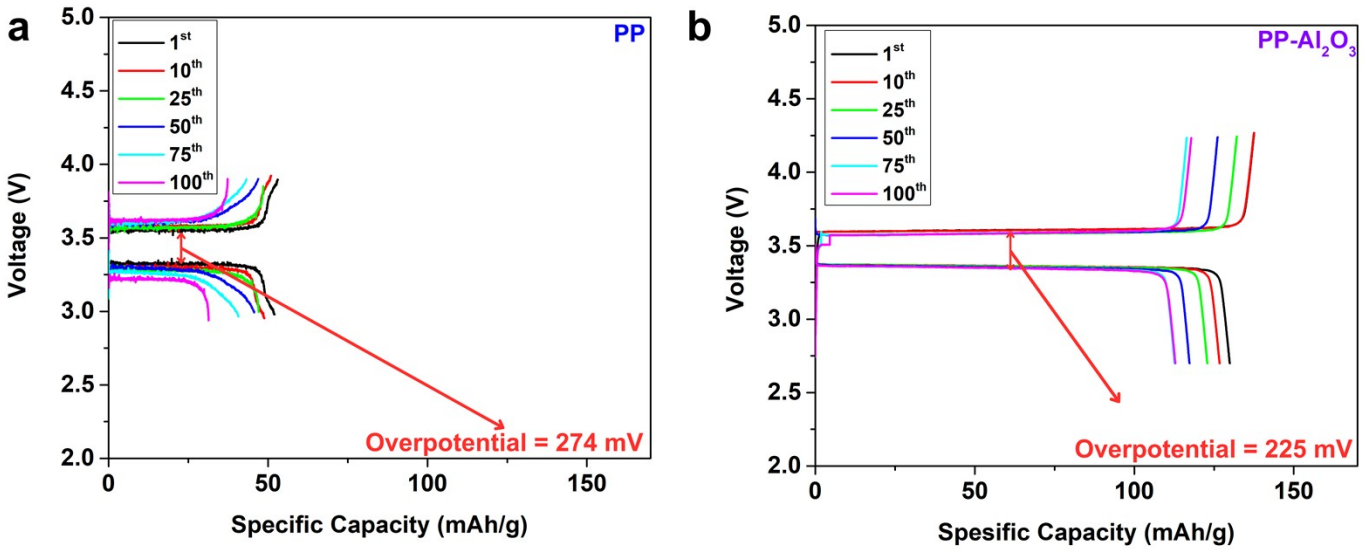

Figure S11. Charge–discharge profiles of full cells using (a) pristine PP and **(b)** PP–Al_2O_3 from the 1st to the 100th cycle.

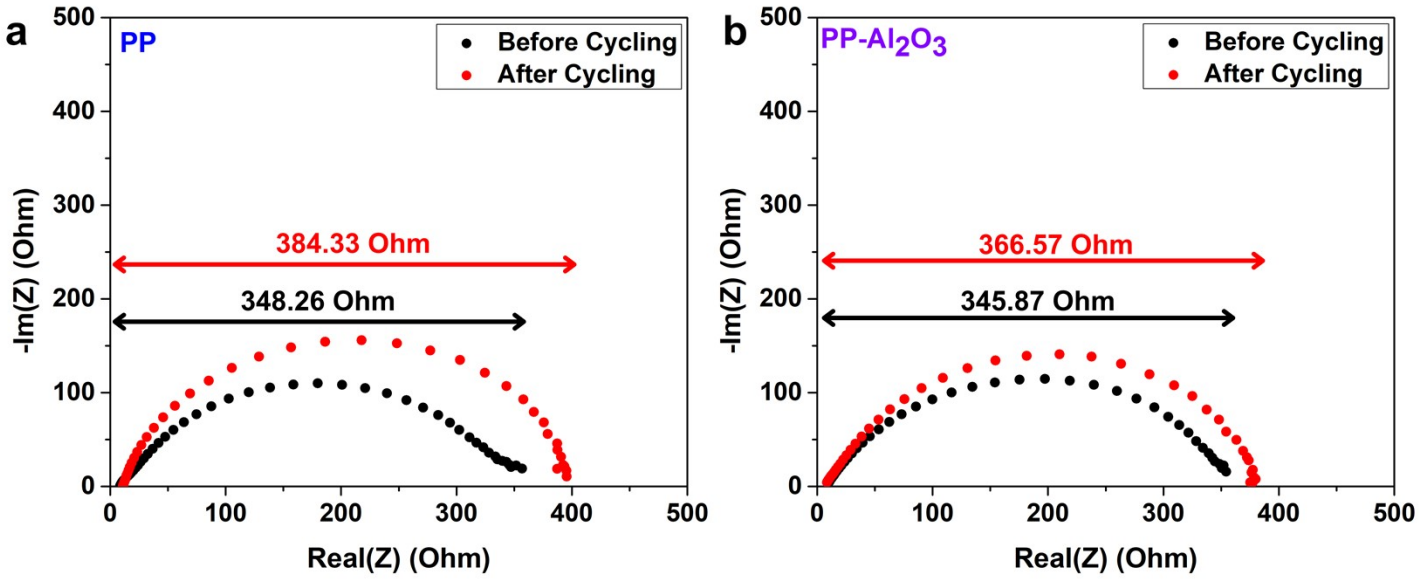

Figure S12. Nyquist plots of full cells using (a) pristine PP and **(b)** PP–Al_2O_3 separators before and after cycling.

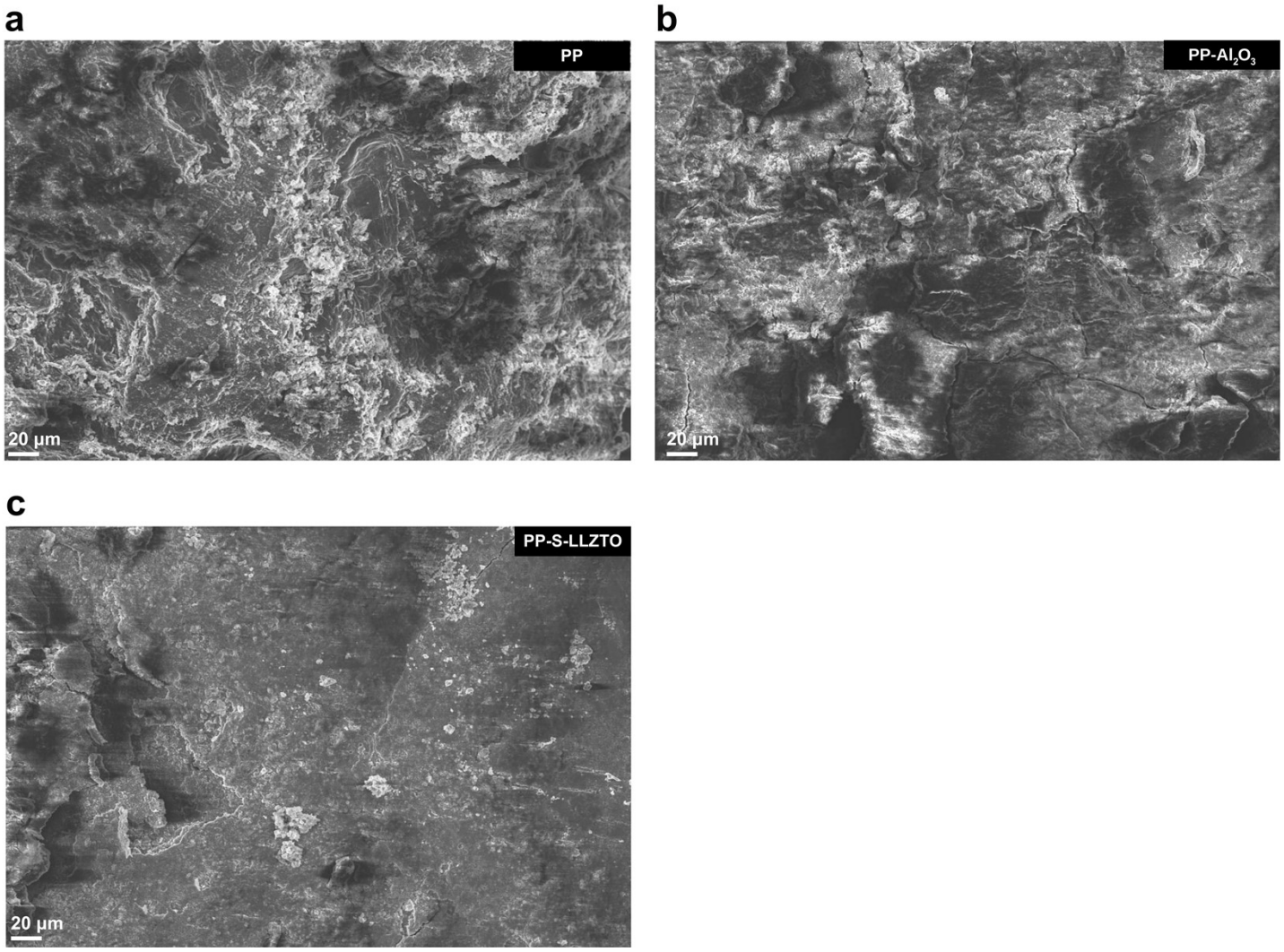

Figure S13. Post-cycling SEM images of Li metal anodes recovered from full cells using **(a)** PP, **(b)** PP–Al_2O_3, and (**c)** PP–S-LLZTO separators.

Table S1. Initial discharge capacities of PP, PP–Al_2O_3, and PP–S-LLZTO separators measured at various C-rates

C-Rate	Initial Capacity Discharge (mAh/g)		
	PP	**PP-Al_2O_3**	**PP-S-LLZTO**
0.2 C	110.93	155.00	165.57
0.5 C	95.65	143.30	150.77
1 C	52.07	129.92	138.01
2 C	39.72	68.78	99.96
0.2 C (recovery)	79.39	148.82	155.49

Table S2. Comparison of quantitative parameters of pristine PP and coated separators.

Quantitative parameters	**PP**	**PP-Al_2O_3**	**PP-S-LLZTO**
Thickness (mm)	0.020	0.022	0.022
Ionic Conductivity (mS/cm)	0.74	0.80	1.43
Electrochemical Stability Window (V)	4	4.1	5.6
Li^+ Transference Number	0.17	0.47	0.56
Thermal Stability (°C)	360	445	490
Porosity (%)	42.58	55.47	63.88
Electrolyte Uptake (%)	117.58	248.59	288.20
Contact Angle in Water (°)	87.32	23.35	8.59
Contact Angle in 1M LiTFSI/TEGDME	29.21°	8.69°	7.21°
Li plating/stripping stability (h)	< 215	< 652	800
Capacity Retention (%)	60.3	84.7	92.7
Initial Capacity @1 C (mAh/g)	52.1	137.6	138.1
Full Cell Overpotential (mV)	274	225	135

Table S3. The properties of surface-coated separators.

Separator	Coating materials	Coating processes	Electrolyte Uptake (%)	Ionic conductivity (mS cm^{-1})	Full cell capacity (mAh g^{-1})	Coating thickness (μm)	Capacity Retention (%)	Ref.
PP (Polypropylene)	S-LLZTO	Blade Coating	288	1.43	138.1 @ 1 C, (LFP|Li)	2	**92.7%**, 100 cycles	This work
PE (Polyethylene)	TiO_2	Dip-coating + hydrothermal growth	269	0.57	86.4 @ 1 C, (LFP|Li)	0.5	82.6% @ 0.5C, 100 cycles	[2]
PP (Polypropylene)	Al_2O_3 (MOA8, 8:1 Al_2O_3/PVDF)	Slurry coating / scraper	218	1.69	127.6 @ 1 C ($LiCoO_2$|graphite)	32	91.1%, 100 cycle	[3]
PE (Polyethylene)	Al_2O_3	Slurry coating	200	0.85	103.02 @ 0.5C ($LiMn_2O4$|graphite)	6	93.6%, 100 cycle	[4]
PP (Polypropylene)	MgSi-PVDF	Slurry coating	267	0.43	160 @0.05C ($LiCoO_2$|Li)	10	88%, 100 cycle	[5]
PP (Polypropylene)	$Ti_{0.6}Fe_{0.4}O_2$	Spraying coating	149	0.93	134.7 @1 C (LFP|Li)	0.72	90.6 %, 100 cycle	[6]
PP (Polypropylene)	Tannic-Acid	Immersed	125	0.46	98.0 @1 C ($LiMn_2O_4$|Li)	-	93.8 %, 200 cycle	[7]
PP (Polypropylene)	PEO/PCL	blade coating	-	0.63	144 @ 1 C (LFP|Li)	1.3	77 %, 800 cycle	[8]

References

1 Y. Meesala, Y. K. Liao, A. Jena, N. H. Yang, W. K. Pang, S. F. Hu, H. Chang, C. E. Liu, S. C. Liao, J. M. Chen, X. Guo and R. S. Liu, *J. Mater. Chem. A*, 2019, **7**, 8589–8601.

2 Z. Chen, T. Wang, X. Yang, Y. Peng, H. Zhong and C. Hu, *Mater.*, 2023, **16**, 2049.

3 E. Shekarian, M. R. J. Nasr, T. Mohammadi, O. Bakhtiari and M. Javanbakht, *J. Nanostructures*, 2019, **9**, 736–750.

4 H. Jeon, D. Yeon, T. Lee, J. Park, M. H. Ryou and Y. M. Lee, *J. Power Sources*, 2016, **315**, 161–168.

5 D. Krasilina, E. K. Khrapova, E. A. Donda, A. A. Grushina, A. M. Rumyantsev, D. A. Kirilenko, N. A. Bert, V. E. Kraft, G. V. Vaganov, E. M. Ivan'kova and A. A. Krasilin, *J. Power Sources*, 2026, **661**, 238677.

6 X. Liang, Y. Zhou, D. Liu, H. Wang, J. Sun and X. Cai, *J. Power Sources*, 2025, **640**, 236765.

7 L. Pan, H. Wang, C. Wu, C. Liao and L. Li, *ACS Appl. Mater. Interfaces*, 2015, **7**, 16003–16010.

8 W. Ye, Z. Fan, X. Zhou and Z. Xue, *Energy Mater.*, 2024, **4**, 400049.